



<http://www.diva-portal.org>

This is the published version of a paper published in *International Journal of Radiation Oncology, Biology, Physics*.

Citation for the original published paper (version of record):

Adjeiwaah, M., Bylund, M., Lundman, J A., Söderström, K., Zackrisson, B. et al. (2019)
Dosimetric Impact of MRI Distortions: A Study on Head and Neck Cancers
International Journal of Radiation Oncology, Biology, Physics, 103(4): 994-1003
<https://doi.org/10.1016/j.ijrobp.2018.11.037>

Access to the published version may require subscription.

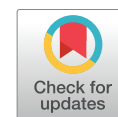
N.B. When citing this work, cite the original published paper.

Permanent link to this version:

<http://urn.kb.se/resolve?urn=urn:nbn:se:umu:diva-157192>

Physics Contribution

Dosimetric Impact of MRI Distortions: A Study on Head and Neck Cancers



Mary Adjeiwaah, MSc, Mikael Bylund, MSc, Josef A. Lundman, MSc,
Karin Söderström, MD, PhD, Prof. Björn Zackrisson, MD, PhD,
Joakim H. Jonsson, PhD, Anders Garpebring, PhD,
and Prof. Tufve Nyholm, PhD

Department of Radiation Sciences, Umeå University, Umeå, Sweden

Received May 14, 2018. Accepted for publication Nov 19, 2018.

Summary

The dosimetric impact of distortions on 21 head and neck cancer magnetic resonance—only radiation therapy treatment plans was studied. Distorted computed tomography (CT) images were obtained by deforming patient CT scans with displacement fields from residual system and patient-induced susceptibility effects. The feasibility of magnetic resonance—only radiation therapy was demonstrated by a dose difference of less than 2% within the target volume for all dosimetric parameters evaluated between distorted CT and CT treatment plans.

Purpose: To evaluate the effect of magnetic resonance (MR) imaging (MRI) geometric distortions on head and neck radiation therapy treatment planning (RTP) for an MRI-only RTP. We also assessed the potential benefits of patient-specific shimming to reduce the magnitude of MR distortions for a 3-T scanner.

Methods and Materials: Using an in-house Matlab algorithm, shimming within entire imaging volumes and user-defined regions of interest were simulated. We deformed 21 patient computed tomography (CT) images with MR distortion fields (gradient nonlinearity and patient-induced susceptibility effects) to create distorted CT (dCT) images using bandwidths of 122 and 488 Hz/mm at 3 T. Field parameters from volumetric modulated arc therapy plans initially optimized on dCT data sets were transferred to CT data to compute a new plan. Both plans were compared to determine the impact of distortions on dose distributions.

Results: Shimming across entire patient volumes decreased the percentage of voxels with distortions of more than 2 mm from 15.4% to 2.0%. Using the user-defined region of interest (ROI) shimming strategy, (here the Planning target volume (PTV) was the chosen ROI volume) led to increased geometric for volumes outside the PTV, as such voxels within the spinal cord with geometric shifts above 2 mm increased from 11.5% to 32.3%. The worst phantom-measured residual system distortions after 3-dimensional gradient nonlinearity correction within a radial distance of 200 mm from the isocenter was 2.17 mm. For all patients, voxels with distortion shifts of more than 2 mm resulting from patient-induced susceptibility effects were 15.4% and 0.0% using bandwidths of 122 Hz/mm and 488 Hz/mm at 3 T. Dose differences between dCT and

Reprint requests to: Mary Adjeiwaah, MSc, Department of Radiation Sciences, Umeå University, SE - 901 87, Umeå, Sweden. Tel: 0046 720 47 415; E-mail: mary.adjeiwaah@umu.se

This work was funded by Schlumberger Faculty for the Future foundation and the Cancer Research Foundation in Northern Sweden.

Conflicts of interest: none.

Supplementary material for this article can be found at <https://doi.org/10.1016/j.ijrobp.2018.11.037>.

Acknowledgments—The authors thank the Schlumberger faculty for the future grants and the Cancerforskningsfond in Norrland for funding the PhD studies of the corresponding author.

Active shimming over entire image volumes reduced distortions resulting from local B_0 -field inhomogeneities. However, shimming over user-defined subvolumes introduced unwanted geometric shifts in nearby regions.

CT treatment plans in D_{50} at the planning target volume were $0.4\% \pm 0.6\%$ and $0.3\% \pm 0.5\%$ at 122 and 488 Hz/mm, respectively.

Conclusions: The overall effect of MRI geometric distortions on data used for RTP was minimal. Shimming over entire imaging volumes decreased distortions, but user-defined subvolume shimming introduced significant errors in nearby organs and should probably be avoided. © 2018 The Authors. Published by Elsevier Inc. This is an open access article under the CC BY-NC-ND license (<http://creativecommons.org/licenses/by-nc-nd/4.0/>).

Introduction

The use of magnetic resonance (MR) imaging (MRI) in the delineation of tumors and organs at risk in the radiation therapy treatment planning (RTP) workflow is increasing. This is largely due to the superior soft tissue contrast provided by MRI, which may reduce potential interobserver variability and uncertainties in delineations.^{1,2} In an 8-year longitudinal study Olmi et al³ reported that in comparison with computed tomography (CT), MRI provided more detailed information on soft tissue invasions beyond the nasopharynx. The use of functional MRI, including diffusion-weighted imaging (DWI) and dynamic contrast-enhanced imaging, in RTP has been shown to identify active tumor subvolumes as potential candidates for dose boosts.⁴⁻⁶ These advantages provided by MRI in RTP have resulted in the proposed MR-only RTP workflow.

Currently, the planning of radiation therapy treatments combines the complementary benefits of MRI and CT through image registration.⁷ MR-CT image registrations allow the delineation of the target volume on MRI data while maintaining the CT electron density information needed for dose calculations. For head and neck RTP, streak artifacts from dental materials on CT images⁸ as well as systematic errors associated with MR-CT image registrations^{9,10} introduce uncertainties with this particular workflow.

An MRI-only RTP workflow¹¹⁻¹⁶ eliminates the use of CT in RTP such that details on a tumor's volume and location as well as the electron density information needed for dose calculations are solely provided by MRI data. Because geometric inaccuracies in radiation therapy images translate to dosimetric uncertainties,¹⁷ MR geometric distortions from system- and patient-related sources challenge the use of MR as the sole input data for RTP. System-related distortions are from inhomogeneities in the main magnetic field and gradient nonlinearities. The magnitude of these distortions increases with distance from the isocenter. Therefore, distortions may be higher for head and neck MRI acquisitions considering the large field of view (FOV) needed for acquiring images in this anatomic region. System-related distortions are machine dependent and can therefore be characterized and possibly corrected for a particular MRI system. Vendor-supplied 3-dimensional

(3D) correction algorithms can be used to minimize gradient-nonlinearity distortions, and passive shimming can be used to reduce magnetic field inhomogeneities.

Patient-related distortions are mainly caused by differences in tissue magnetic susceptibilities within the patient. Susceptibility-induced distortions are greater at higher magnetic field strengths. Of particular concern to head and neck cancer MRI-only RTP are differences in magnetic susceptibility at the interfaces among tissue, dental materials, air cavities, and bony structures in this region. These disturb the homogeneity of the main magnetic field,^{18,19} leading to distortions. Spatial shifts resulting from magnetic field inhomogeneities can be minimized by increasing bandwidth (BW), but high BW lowers the signal-to-noise ratio (SNR). It is possible to compensate for patient-induced B_0 -field inhomogeneities through active magnetic field shimming.^{20,21} Here, the magnetic field homogeneity can be optimized for entire imaging volumes within the FOV or a user-defined region of interest (ROI).^{22,23} Shimming based on user-defined ROI, especially in regions of increased tissue magnetic susceptibility differences, may be beneficial. However, this approach leads to increased frequency offsets generated in voxels outside the user-defined ROI with increasing shim orders.

Several studies have isolated the effect of MRI's spatial inaccuracies on prostate cancer RTP,^{14,16,24-26} showing dose differences of less than 2.0% between MRI- and CT-based treatment plans. These studies were done in a region where the anatomic volume of interest is situated at the center of the FOV,²⁷ where system distortions are negligible. In addition, tissue magnetic susceptibility differences in this region are minimal compared with the head and neck area. Mohammed et al²⁸ characterized MRI distortions in the head and neck region and reported distortions of less than 2 mm but did not evaluate their dosimetric impact on RTP.

In this work, we characterized patient-induced susceptibility distortions using a method by Lundman et al²⁹ that uses CT images. The CT images were for patients with oropharyngeal and oral cavity cancers included in the prospective Swedish phase 3 multicenter randomized control study, ARTSCAN.³⁰ We investigated the combined effect of simulated patient-induced susceptibility effects and phantom-measured residual MRI system distortions after 3D gradient nonlinearity correction on head and neck

RTP at 3 T. Shimming on a modern scanner could be done either over the entire imaging volume or over a user-defined volume. Our first step was to identify the most clinically relevant strategy for this treatment region. We then performed the dosimetric evaluation for that scenario. An in-house shimming algorithm was used to generate the correction field needed to optimize the B_0 field homogeneity across entire imaging volumes and within a user-defined ROI. The delineated planning target volume (PTV) was chosen as the user-defined shimming volume.

Methods and Materials

Distortion quantification: Gradient nonlinearity

A commercial large FOV 3D phantom (GRADE Phantom by Spectronic Medical AB, Helsingborg, Sweden)²⁴ was scanned with a 3.0-T GE SIGNA positron emission tomography/MR system (GE Healthcare, Milwaukee, WI) to measure residual gradient nonlinearity distortions after using the vendor-supplied 3D distortion correction algorithm. The Gradwarp (GE Healthcare, Waukesha, WI) algorithm that was enabled by default only corrects for gradient nonlinearity distortions in-plane; to correct for distortions in the slice direction, the option “3D Geometry Correction” was enabled for all phantom scan acquisitions.³¹ The 3D geometry correction can be used for 3D and 2-dimensional (2D) sequences without slice gaps.³¹

A T2-weighted fast spin-echo sequence with a repetition time of 1500 milliseconds, an echo time of 99 milliseconds, and a 500-mm FOV was used to acquire $0.98 \times 0.98 \times 2 \text{ mm}^3$ axial images of the phantom with no slice gaps. BWs of 122 and 488 Hz/mm were used for the MR image acquisitions and the patient-induced susceptibility simulations to illustrate the effects of BW on the magnitude of MRI geometric distortions.

For the system distortion analysis, the phantom images were uploaded to a cloud-based analysis software. The system automatically estimated the marker displacements by using a nonrigid image registration between the uploaded images and a digital reference model of the phantom.²⁴ The result of this analysis was a displacement vector field map showing the difference in marker positions calculated by inverse mapping.³²

We used patient CT images from the prospective Swedish phase 3 multicenter randomized control study, ARTSCAN,³⁰ to estimate patient-induced susceptibility effects. All patients were scanned in the supine head-first position either on a Philips Brilliance Big Bore (120 kV voltage, 113-320 mA tube current) using an in-plane resolution of $1.07 \times 1.07 \text{ mm}^2$ or a Siemens Emotion 6 (130 kV voltage, 88 mAs tube current) CT camera with a resolution of $0.97 \times 0.97 \text{ mm}^2$. All patient scans had an image matrix of 512×512 .

Distortion quantification: Patient-induced susceptibilities

We estimated patient-induced susceptibility distortions using a previously described methodology,^{14,29} where magnetic susceptibility (χ) values were assigned to segmented tissues based on their CT Hounsfield unit (HU) values. The segmented tissues and their assigned HU and magnetic susceptibility values were air [HU: -1000, $\chi(10^{-6})$: 0.36]¹⁸; fat [HU: -120, $\chi(10^{-6})$: -7.79]³³; muscle [HU: 100, $\chi(10^{-6})$: -9.05]¹⁸; and bone [HU: 700, $\chi(10^{-6})$: -11.30].³³ The CT images were converted to susceptibility maps. The susceptibility map therefore represented the distribution of magnetic susceptibility values for each patient.

The input parameters to the induced susceptibility algorithm were the image matrix together with the magnetic susceptibility map and patient mask.²⁹ Also specified was the pixel BW in the frequency encoding direction. The simulation produced the local B_0 field homogeneity distribution, distortion field, and the distorted CT image. The output data had the same DICOM coordinates as the input patient CT.

To account for susceptibility effects resulting from dental fillings, the susceptibility value of gold, -34×10^{-6} ,¹⁸ was assigned to contoured dental fillings of 9 patients. Gold has been shown to produce significant distortions in dental MRI.³⁴ Areas with severe streak artifacts were contoured and assigned the CT number of soft tissues. The readout for induced susceptibility simulations were in the anteroposterior direction to minimize pulsation artifacts.

Patient-specific shimming simulation

Active shimming mainly corrects for patient-induced field inhomogeneities. To simulate active shimming, we started by obtaining maps of the local B_0 field owing to magnetic susceptibility differences using the method by Lundman et al²⁹ as described earlier. An in-house Matlab algorithm was used to calculate the optimal shim parameters needed to improve the magnetic field homogeneity (the code can be found in the Appendix A.1.; available online at <https://doi.org/10.1016/j.ijrobp.2018.11.037>). In the optimization, it was assumed that the shim coils could produce fields corresponding to spherical harmonics (SH) functions.³⁵ Thus, the shim fields were given by

$$B_{\text{shim}}(\mathbf{x}) = \sum_{l=0}^N \sum_{m=-N}^N c_{lm} Y_l^m(\mathbf{x}) \quad (1)$$

where N was the shim order, and $Y_l^m(\mathbf{x})$ and c_{lm} were the SH basis functions and the coefficients calculated when optimizing the shimming.

For this study, shim-field coefficients across entire imaging volumes (Fig. 1a) and within a user-defined ROI (Fig. 1b) at first and second shim orders were optimized. The selected user-defined ROI for this study was the

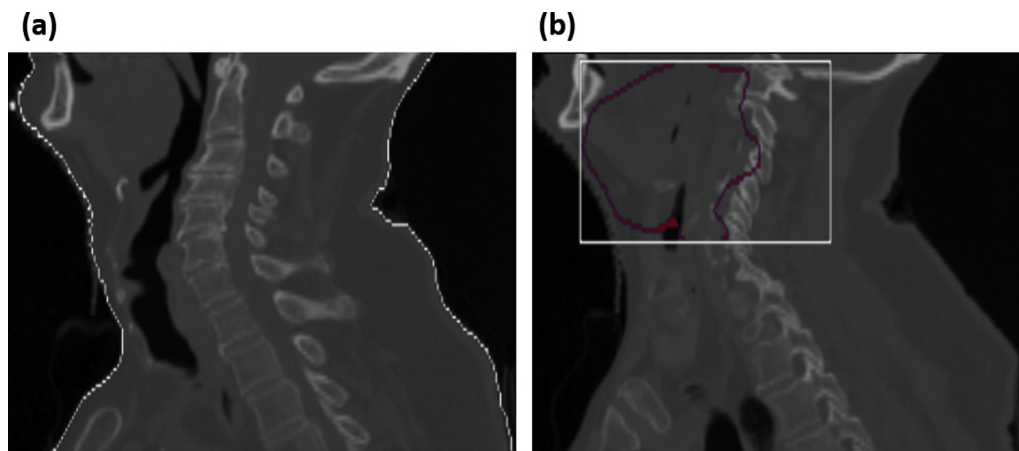


Fig. 1. Shimming methods used in this study. Magnetic field optimizations were done within the entire imaging volume (a) and a user-defined region of interest (b), which was the planning target volume. The user-defined region of interest volume for all patients was a bounding box (white) covering the delineated planning target volume (pink). (A color version of this figure is available at <https://doi.org/10.1016/j.ijrobp.2018.11.037>.)

contoured PTV. The aim of the user-defined ROI shimming strategy was to quantify the worsening field variations that occur in voxels not included in the selected shimmed ROI, as shown in Figure 1b. To do this, a mask defining a bounding box around the contoured PTV was initially created. The region defined by the bounding box, which covered the delineated PTV, was shimmed for all 21 patients.

The local B_0 -field homogeneity values for all patient voxels based on the 2 shimming approaches were estimated based on geometric shifts (z) in millimeters at the studied BWs for a 3-T system using Equation 2.³¹

$$z(mm) = \frac{\Delta B_0(ppm) \times 42.58(MHz/T) \times 3T}{BW(Hz/mm)} \quad (2)$$

Distorted CT image generation

Distorted CT (dCT) images were generated by deforming patient CT images with combined displacement fields from the phantom-measured residual gradient nonlinearity distortions and simulated patient-induced susceptibility effects. Initially, data from the patient-induced susceptibility effects were corrected for B_0 field inhomogeneities through whole image volume shimming. This was the shimming strategy found to be most clinically relevant. In addition, the acquisition sequence for the phantom images has automatic shimming within the imaging FOV.

Because the distortion maps from the MR scanner were not in the same frame of reference as the patient CT images, they were initially translated and resampled to match the CT DICOM image coordinates and resolution. As a result, the 2 image data sets were aligned and centered similarly on both the MRI and CT. Alignment (center-to-center translation) was done in such a way that the CT images were positioned at the center of the MR distortion fields. By so doing, we minimized gradient nonlinearity

effects while maximizing field homogeneity. The vector fields from patient-induced susceptibility effects and the now translated residual gradient nonlinearity distortions were added and used to deform the patient CT data. The deform function, based on the Insight Segmentation and Registration Toolkit's (ITK) WarpImageFilter, warps an input image with respect to the supplied displacement field.³⁶ All delineated structures were also deformed.

We estimated the magnitude of distortions at the delineated PTV, spinal cord, brain, and parotid glands. The Dice similarity coefficient (DSC) was used to assess variations in contour overlaps between dCT and CT data sets.³⁷ A DSC value of 1 shows perfect agreement, whereas 0 denotes no overlap. The induced susceptibility effect simulation and dCT creation were done with MICE-Toolkit (NONPI Medical AB, Umeå, Sweden), a medical image analysis software.

Treatment planning

Oncentra External Beam version 4.5 (Elekta, Stockholm, Sweden) was used for all dose calculations. Dual-arc, 6-MV volumetric modulated arc therapy plans were initially optimized on dCT data after whole volume shimming. The volume of interest for the treatment planning represented patients with oropharyngeal and oral cavity targets. All patients had 68 Gy prescribed to the PTV surrounding the microscopic tumor, PTV_{tumor} (referred to as PTV throughout this paper).³⁰ Elective doses of 46 Gy and 54 Gy in 2 Gy per fraction were prescribed for 17 and 4 patients, respectively. Dose calculations were done with pencil beam algorithm using a dose grid resolution of $2 \times 2 \times 2$ mm³. The isocenter of the beam was placed at the center of the PTV in the undistorted data sets.

To isolate the effect of distortions on dose distribution, the beam arrangements from the optimized dCT plan were exported and subsequently imported onto the undistorted

patient CT data sets. A new dose distribution was calculated with no changes to the beam weights, monitor units, and dose grid resolutions. No optimization was done at this stage.

Eighty-four treatment plans based on the 2 BWs were made for the 21 patients (42 dCT and 42 CT). The acceptance criteria for the treatment plans were as follows:

1. The minimum dose to the clinical target volume shall be $\geq 95\%$ of the prescribed dose (PD), $D_{\min} \geq 95\%$ of PD.
2. The 95% isodose shall cover at least 95% of the PTV, $V_{95\%} \geq 95\%$.
3. Maximum dose to the spinal cord as the planning at risk volume shall be $< 70\%$ of PD.

We analyzed the dose distributions from all treatment plans based on the following parameters:

1. Median (D_{50}), maximum (D_{\max}), and minimum (D_{\min}) dose to the PTV, spinal cord, and right and left parotids
2. Near minimum ($D_{98\%}$) and near maximum ($D_{2\%}$) dose to the PTV as well as the 95% isodose that covered at least 95% of the PTV ($V_{95\%}$)

The percentage dose difference at the studied BWs between the optimized dCT and CT treatment plans based on the aforementioned parameters was calculated as:

$$\Delta D = \frac{dCT - CT}{dCT} \times 100\% \quad (3)$$

Dose reporting was made according to the recommendations of the International Commission on Radiation Units.³⁸ All statistical analysis and plots were done with MATLAB R2016b (The MathWorks, Inc., Natick, MA).

Results

Distortion quantification

The largest observed distortions at 3 T measured with the phantom after 3D gradient nonlinearity correction at a radial distance of 200 mm using BWs of 122 and 488 Hz/mm were 2.17 (mean, 0.76 mm) and 2.15 mm (mean, 0.64 mm), respectively. For all patients, voxels with distortion shifts > 2 mm resulting from patient-induced susceptibility effects were 15.4% and 0.0% using BWs of 122 Hz/mm and 488 Hz/mm at 3 T. The majority of voxels with high distortions were located in regions with dental fillings and areas surrounded by air.

The combined distortions from the phantom-measured and patient-induced susceptibility effects are presented in Table 1. Also displayed in Table 1 are the mean DSC values and the volume of the undistorted CT structures. We found patient-induced susceptibility effects were the largest contributor to the total geometric distortions at the studied structures. Increasing BW resulted in reduced distortions and better overlap between dCT and CT contours.

Patient-specific shimming

Shimming over entire imaging volumes

Using the SH shimming model to optimize magnetic field variations improved the overall homogeneity of the B_0 field. Illustrated in Figure 2 is the reduction in magnetic field inhomogeneity values with increasing shim orders for 9 representative patients. The majority of the voxels had absolute homogeneity values within 5 ppm after shimming. A narrower histogram peak as observed in most of the first- and second-order shimming histograms was an indication of reduced magnetic field variation. From

Table 1 Total geometric shifts at 3 T from phantom measured residual system distortions corrected for gradient nonlinearity effects and patient-induced susceptibility distortion at the contours of the PTV, spinal cord, right and left parotids, and brain

Contoured structures	BW (Hz/mm)	Maximum distortion range (mm)	Mean distortion range (mm)	Undistorted CT volume (cm ³)	Mean DSC \pm 1 SD
PTV	122	3.5-5.5	0.7-2.9	148.4-659.6	0.95 \pm 0.02
	488	1.0-1.6	0.2-0.8		0.99 \pm 0.01
Brain	122	1.1-5.1	0.8-1.2	653.0-883.3	0.97 \pm 0.02
	488	0.5-1.9	0.4-0.9		0.99 \pm 0.01
Left parotid	122	1.8-4.0	0.7-2.1	11.4-34.0	0.91 \pm 0.03
	488	0.4-0.9	0.2-0.6		0.99 \pm 0.01
Right parotid	122	1.5-3.5	0.6-2.3	8.3-36.9	0.90 \pm 0.03
	488	0.5-1.2	0.2-0.8		0.97 \pm 0.01
Spinal cord	122	2.2-4.8	0.9-2.0	9.9-67.7	0.85 \pm 0.06
	488	0.7-1.3	0.3-0.5		0.97 \pm 0.01

Abbreviations: BW = bandwidth; CT = computed tomography; DSC = Dice similarity coefficient; PTV = planning target volume; SD = standard deviation.

The undistorted CT volume of the contoured structures are also shown. Comparison of overlap between the contours of 3-T distorted and undistorted CT data for all patients is displayed as the DSC. Data are represented as the range in maximum and mean values.

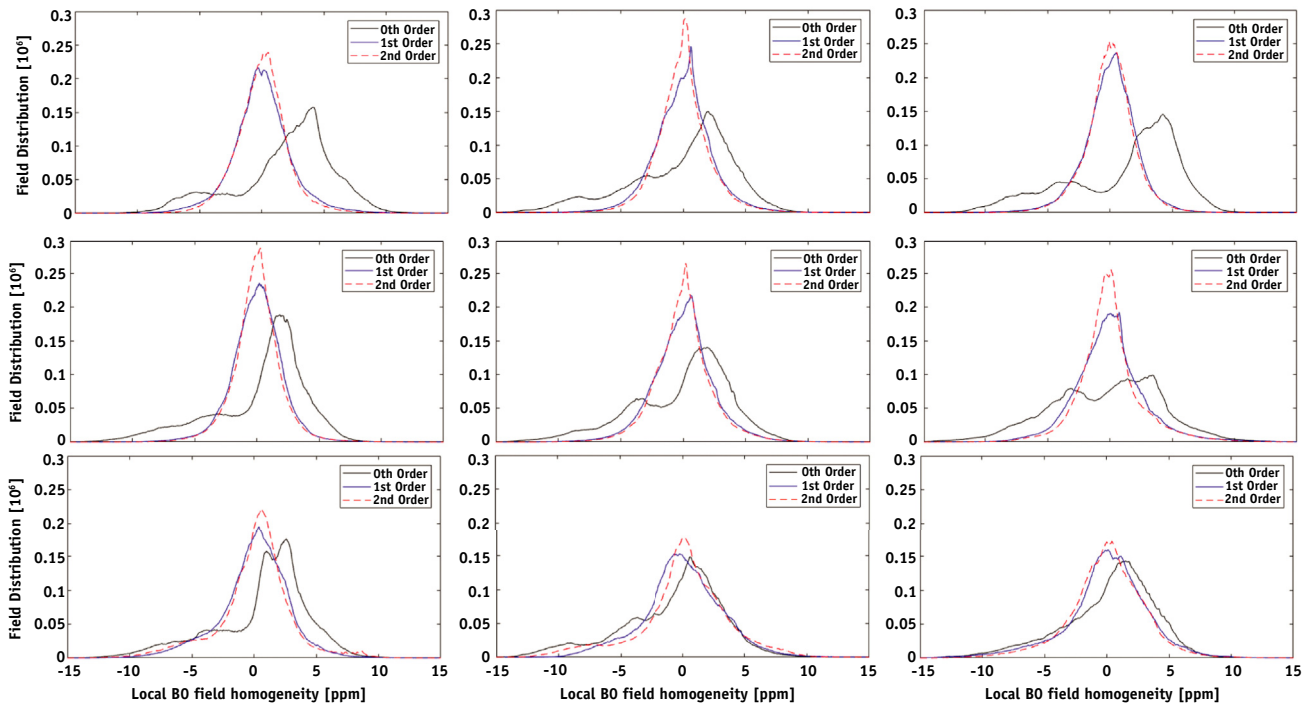


Fig. 2. A histogram showing the distribution of magnetic field variations before and after shimming across the entire imaging volume of 9 patients. The first 2 rows are for patients with contoured dental fillings, and the last row is for patients without dental fillings. The shift of the histogram peaks to center around 0 after first- and second-order shim, is an indication of increased field homogeneity.

Figure 2, it can be inferred that second-order shimming did not significantly improve the magnetic field homogeneity after first-order shimming. Shimming across entire imaging volumes reduced the number of voxels with geometric shifts exceeding 2 mm from 15.4% before shimming to 2.7% and 2.0% after first- and second-order shimming, respectively, at 122 Hz/mm for 3 T. At the same field strength but with a BW of 488 Hz/mm, voxels with geometric shifts >2 mm were 0.0% before optimization with no significant changes after shimming.

User-defined ROI shimming

A box plot to compare the voxel-by-voxel geometric shifts resulting from field inhomogeneities within and outside the user-defined ROI for all patients before and after shimming at 3 T is illustrated in Figure 3. From Figure 3, the interquartile range at 122 Hz/mm at the zeroth, first- and second-order shimming within the shimmed ROI were 1.28 mm, 0.77 mm, and 0.50 mm. The corresponding values for all voxels excluding the user-defined shimmed ROI were 1.79 mm, 3.90 mm, and 6.53 mm after 0th, first, and second shim orders, respectively. At 488 Hz/mm, the estimated values were 0.32, 0.19, and 0.13 for voxels within the ROI and 0.40, 0.98, and 1.63 for voxels outside the user-defined shimmed ROI at 0th, first, and second shim orders.

Table 2 shows the rise in the number of voxels with geometric shifts more than 2 mm for some selected contours after optimizing field homogeneity within the contours of the PTV. A decrease in magnetic field

inhomogeneities within the PTV resulted in as much as 56.0% of the voxels within the contoured brain having geometric shifts more than 2 mm.

Dosimetric evaluation

The dose difference in percent for $D_{2\%}$, $D_{98\%}$, and V_{95} at the PTV based on dCT and CT treatment plans were $0.1\% \pm 0.6\%$, $0.7\% \pm 1.0\%$, and $0.2\% \pm 0.7\%$, respectively, at 122 Hz/mm. The corresponding values obtained at 488 Hz/mm were $0.0\% \pm 0.3\%$, $0.6\% \pm 0.6\%$, and $0.2\% \pm 0.3\%$, respectively. Table 3 shows the percentage difference in dose at the PTV and some delineated organs at risk between dCT and CT treatment plans based on a 3-T system. At the PTV, a mean dose difference of less than 1% between dCT and CT plans in D_{50} was obtained across all patients. On average, the 95% isodose covered PTV volumes of $98.4\% \pm 0.7\%$ and $98.2\% \pm 0.6\%$ on dCT and CT plans. Two patients did not fulfill the plan acceptance criteria on either the dCT or CT treatment plans. For these patients, less than 95% of their PTV volume was covered by the 95% isodose for both BWs. Between the 2 patients, one did not fulfill any of the plan acceptance criteria on either plan.

Discussion

We have demonstrated that by using an appropriately high BW of 488 Hz/mm combined with 3D gradient nonlinearity

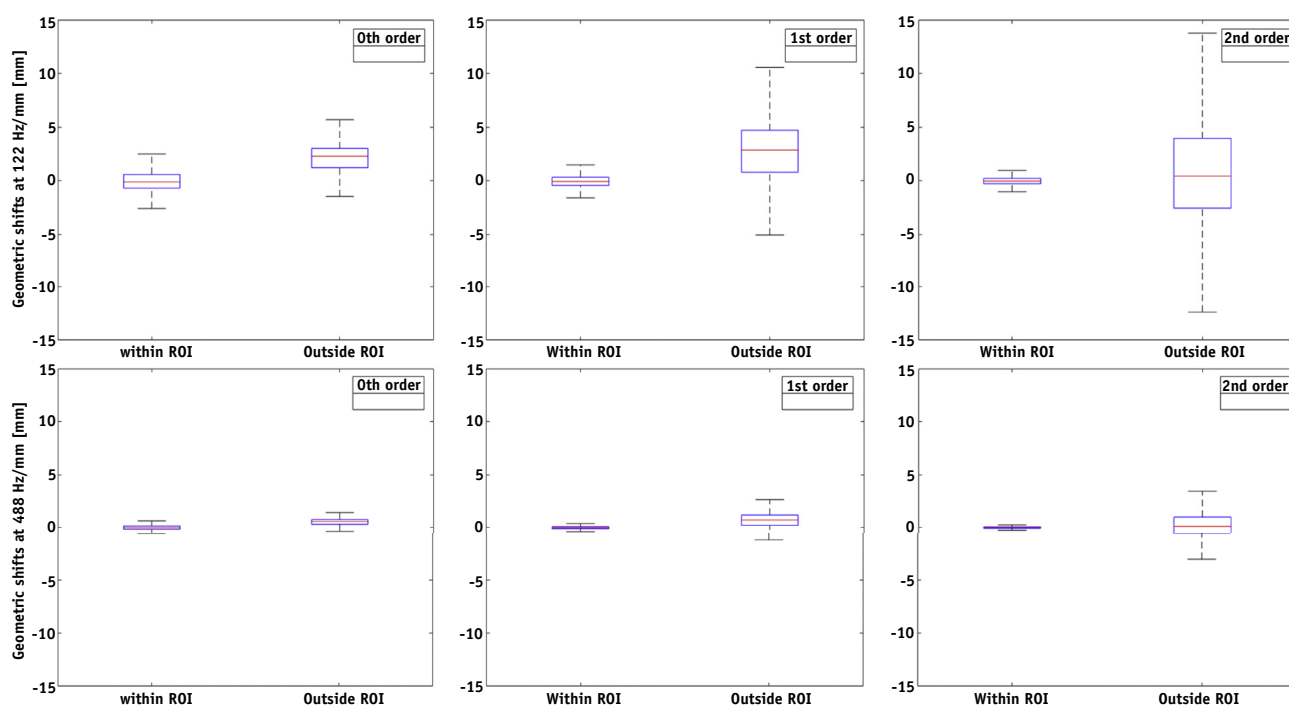


Fig. 3. Optimizing the shim parameters within a user-defined region of interest (ROI) compromises the B_0 -field homogeneity of voxels outside the shimmed volume. A box plot of the voxel-by-voxel B_0 -field homogeneity levels for all the 21 patients studied. Compared at each shim order is the 3-T geometric shift (in mm) at 122 and 488 Hz/mm for all voxels within and outside the user-defined shimmed ROI. For each box, the central mark is the median, whereas the bottom and top of the central box are the first and third quartiles. There was a decrease in geometric shifts inside the shimmed ROI after first- and second-order shimming, whereas the opposite effect was observed in voxels outside the shimmed volume. Here, 0th order is the unshimmed B_0 -field due to patient-induced susceptibility effects.

correction and shimming whole image volumes, dosimetric quality measures including D_{50} , $D_{2\%}$, D_{max} , and $V_{95\%}$ at the PTV between dose distributions based on distorted and undistorted data sets can be kept within 1%. Our findings are consistent with the results of previous investigations on the effect of distortions on dose distributions at different anatomic sites, where a dose difference of less than 2% has been found between MRI and CT RTP.^{14,16,24,25,27,39,40} We also showed that user-defined ROI shimming elevates the magnitude of distortion shifts in nearby regions not included in the shimmed volume.

To achieve accurate spatial encoding in MRI, a homogeneous static magnetic field combined with linear gradient systems is required. The design of MRI systems is such that imperfections in the main magnet's field homogeneity exist and nonlinearities in the gradients escalate with increasing radial distance from the magnet's isocenter. Thus, larger system distortions may be measured if the shoulders, especially of larger patients, are included in the RTP of head and neck cancers. Such a scenario was not investigated in this current study. The potential effect on dose distributions as reported by Chin et al⁴¹ is such that for a single 6-mV radiation field treating a depth of 6 cm, a difference of 4 mm of tissues could result in a 2% dose difference. To reduce the dose difference to 0.5%, Chin et al⁴¹ used multiple field arrangements to avoid the

shoulders.⁴¹ A FOV between 200 and 250 mm may provide the needed anatomy required for delineations and contouring for most head and neck RTP purposes.⁴²

Table 2 The number of voxels with geometric shifts >2 mm for all patients before and after optimizing the magnetic fields within the contoured PTV

Contoured structures	BW (Hz/mm)	Before shimming	After shimming	
		0th order (%)	First order (%)	Second order (%)
PTV	122	3.85	2.64	1.28
	488	0.00	0.00	0.00
Brain	122	42.00	48.36	55.95
	488	0.00	0.00	7.74
Left parotid	122	0.050	0.20	2.20
	488	0.00	0.00	0.00
Right parotid	122	0.003	1.65	3.80
	488	0.00	0.00	0.00
Spinal cord	122	11.48	21.42	32.25
	488	0.00	0.37	5.40

Abbreviations: BW = bandwidth; PTV = planning target volume.

The PTV was the user-defined shimmed region of interest. The results presented in percentages are for a 3-T scanner using BWs of 122 and 488 Hz/mm.

Table 3 Comparison of percentage differences for the minimum (D_{\min}), median (D_{50}), and maximum (D_{\max}) dose values between volumetric modulated arc therapy treatment plans optimized on the 3-T dCT and the recalculated plans on the undistorted patient CT data sets

Contoured structures	BW (Hz/mm)	D_{\min} (%)	D_{50} (%)	D_{\max} (%)
	PTV	122	0.70 ± 0.91	0.38 ± 0.59
	488	0.53 ± 0.73	0.34 ± 0.53	-0.07 ± 0.84
Left parotid	122	1.48 ± 2.25	0.43 ± 1.25	0.51 ± 1.39
	488	1.47 ± 1.62	0.12 ± 1.11	0.18 ± 0.81
Right parotid	122	1.94 ± 1.93	0.25 ± 1.84	0.13 ± 0.96
	488	1.37 ± 1.64	0.23 ± 1.74	0.11 ± 0.91
Spinal cord	122	0.96 ± 1.78	1.37 ± 1.89	-0.48 ± 1.90
	488	0.10 ± 1.89	0.93 ± 1.77	-0.21 ± 1.85

Abbreviations: BW = bandwidth; CT = computed tomography; dCT = distorted computed tomography; PTV = planning target volume.

Magnetic field variations come not only from imperfections in the MRI scanner hardware but also from the patient as a result of magnetic susceptibility and chemical shift effects. Chemical shift results in the displacement of fatty tissue and could therefore be seen as causing artifacts and not necessarily geometric distortions in the same sense as susceptibility effects. In MRI, the most prominent chemical shift in the human anatomy is between the protons in water and fat, which is about 3.5 ppm, translating to Larmor frequency shifts of 440 Hz at 3 T. The heterogeneity at the borders among air, tissue, dental materials, and bone resulted in 42.0%, 11.5%, and 3.9% of the voxels in the brain, spinal cord, and PTV, respectively, having distortion shifts of more than 2 mm at 122 Hz/mm.

The relevance of using high BW to reduce the magnitude of distortions is shown in Table 1, where increasing BW from 122 Hz/mm to 488 Hz/mm contributed to a commensurate decrease in the magnitude of total distortions. By using a BW of 488 Hz/mm at 3 T, voxels with geometric shifts of more than 2 mm were reduced to 0, as shown in Table 2. Aside from these structures, only a negligible number of voxels (0.0%) that were within the patient's external body contour had voxel shifts exceeding 2 mm at 3 T using a BW of 488 Hz/mm.

Wang et al⁴³ characterized patient-induced susceptibility distortions in clinical brain images from a 3-T scanner using magnetic field inhomogeneity mapping. They reported that only 0.1% of the displacements were more than 2 mm for a BW of 180 Hz/pixel, but displacements of up to 4 mm were found.⁴³ If all scan acquisition parameters are kept constant, then increasing pixel BW not only reduces the magnitude of distortions but can lead to faster image acquisitions. As increasing BW is restricted by SNR, high BW sequence protocols that fulfill the SNR requirements of

the MR images are to be used for RTP image acquisitions.⁴⁴ For RTP purposes, a BW of at least twice the water-fat shift per pixel has been recommended.⁴² The assumption is that, at this BW, the magnetic susceptibility-field offsets will be within twice the water-fat separation. According to our results a lower BW of around 440 Hz/mm at 3 T will result in very small dosimetric errors for the investigated treatment strategy.

Passive and active shimming strategies can be used to reduce distortions due to magnetic field inhomogeneities. Even for a perfectly shimmed magnet, the introduction of a patient into the scanner causes variations in the magnet's field homogeneity. Thus, for most applications the results of active shimming may be more relevant than the homogeneity of the empty magnet. Active shimming involves combining a set of basis functions such as SH to reduce field inhomogeneities caused by differences in tissue magnetic susceptibility. As illustrated in Figure 2, shimming across the entire imaging volume resulted in the narrowing of the histogram peaks, after first and second shim orders signifying improvements in the local B_0 -field homogeneity. This is contrary to the observations made in Figure 3, where the optimization of field parameters within a selected region resulted in increased distortion shifts outside this region. Furthermore, by assigning susceptibility values to contoured dental fillings, an absolute maximum local B_0 -field homogeneity value of 15 ppm within the entire imaged volume was obtained. It must, however, be pointed out that this was an extreme value; the majority of the voxels had values within ± 5 ppm, as displayed in Figure 2. Our findings are in line with what has been previously reported.^{18,45-48}

The use of user-defined ROI shimming over the intended imaging volume may be performed at anatomic regions vulnerable to highly induced magnetic susceptibility effects, such as the head and neck region. This compensates for B_0 -field variations while avoiding distortions within the shimmed ROI. However, during the optimization process the fields are added globally and can result in increased magnetic field inhomogeneities outside the shimmed volume. Additionally, if high-order shimming is used, then complex field inhomogeneities within the optimizing volume would have to be minimized, which could potentially increase the size of distortions in voxels outside the user-defined shimmed ROI.⁴⁹ The clinical implication is that in a typical head and neck RTP, the target volume may be surrounded by critical organs such as the spinal cord. Therefore, shimming the target volume in order to minimize spatial inaccuracies may lead to positional mismatch between these anatomic structures on the MR images and their corresponding position within the patient. Methods such as dynamic^{21,50-52} and cost function-guided⁵³ shimming have been used to minimize the degradation of field homogeneity in voxels outside the shimmed ROI for MR spectroscopy applications.

In this study, the magnetic field disturbances were modeled to originate from the patient only, which is a

simplification because other possible sources were ignored. However, under normal circumstances, the patient is the main source of B_0 disturbances, and the results should therefore be realistic. The measurement of the B_0 field is also crucial, and in this work we have assumed that the measurements were perfect. In reality there can be deviations, which are likely to depend on the particular shimming algorithm used. However, evaluating the different B_0 measurement techniques was outside the scope of this work, and the results here should therefore be viewed as what can be achieved with an ideal B_0 measurement.

Another shimming method available for magnetic field inhomogeneity correction is the FASTMAP shimming technique,⁵⁴ where B_0 field maps are measured along 6 projections.

This study did not consider dental implants and crowns or other metallic orthodontic materials that, based on their geometry, size, and make, may generate larger distortions compared with dental fillings. As an example, titanium, a popular material for dental implants, has a susceptibility value of 182×10^{-6} ,¹⁸ which will result in a greater titanium/tissue magnetic susceptibility difference in comparison with gold and air or gold and tissue. There is the possibility of using active shimming to reduce this effect. However, this might be a complicated process because it must be done at every treatment angle; this would require further investigations. The phantom-measured system-related distortions were from only 1 scanner. However, the reproducibility and sensitivity of similar phantoms by the same vendor has been reported by Wyatt et al⁵⁵ for 3 MRI systems. We did not consider object-induced distortions from the phantom material. It has been reported to be <0.5 mm at radial distances <250 mm from the magnet's isocenter measured at 554 Hz/mm.²⁴ Because object-induced distortions cannot be reduced with gradient nonlinearity correction algorithms, they may have contributed significantly to the overall system-related distortions, especially at the lowest BW (122 Hz/mm) used in this study.

Conclusions

This work used CT images distorted with combined distortion fields from phantom-measured MRI residual gradient nonlinearity and simulated patient-induced susceptibility distortions from a 3-T scanner. We have demonstrated that within the target volume and nearby organs at risk, the dosimetric impact of MRI distortions is small for a high-BW spin echo sequence. Considering the increase in scanners with high field strengths and the lack of vendor-specific correction algorithms for patient-related distortions, high BW and shimming across entire imaging volumes could be beneficial for RTP applications. Worsening field variations observed in voxels outside the shimmed ROI during user-defined ROI shimming would

require careful consideration, and such a shimming strategy should probably be avoided.

References

1. Fiorino C, Reni M, Bolognesi A, Cattaneo GM, Calandrino R. Intra- and inter-observer variability in contouring prostate and seminal vesicles: Implications for conformal treatment planning. *Radiother Oncol* 1998;47:285-292.
2. Villeirs GM, Van Vaerenbergh K, Vakaet L, et al. Interobserver delineation variation using CT versus combined CT + MRI in intensity-modulated radiotherapy for prostate cancer. *Strahlentherapie und Onkol* 2005;181:424-430.
3. Olmi P, Fallai C, Colagrande S. Staging and follow-up of nasopharyngeal carcinoma: Magnetic resonance imaging versus computerized tomography. *Int J Radiat Oncol Biol Phys* 1995;32:795-800.
4. Thorwarth D. Functional imaging for radiotherapy treatment planning: Current status and future directions—A review. *Br J Radiol* 2015;88:20150056.
5. Tsien C, Cao Y, Chenevert T. Clinical applications for diffusion magnetic resonance imaging in radiotherapy. *Semin Radiat Oncol* 2014;24:218-226.
6. Bhatnagar P, Subesinghe M, Patel C, Prestwich R, Scarsbrook AF. Functional imaging for radiation treatment planning, response assessment, and adaptive therapy in head and neck cancer. *Radiographics* 2013;33:1909-1929.
7. Köhler M, Vaara T, Van Grootel M, Hoogeveen R, Kemppainen R, Renisch S. MR-only simulation for radiotherapy planning treatment planning. Philips MRCAT Prostate Dose Calculated Using Only MRI Data, White Paper; 2015;:1-16.
8. Lee M, Kim S, Song H, Huh Y, Han S, Suh J. Overcoming artifacts from metallic orthopedic implants at high-field-strength MR imaging and multi-detector CT. *Radiographics* 2007;27:791-804.
9. Ulin K, Urie MM, Cherlow JM. Results of a multi-institutional benchmark test for cranial CT/MR image registration. *Int J Radiat Oncol Biol Phys* 2010;77:1584-1589.
10. Brock KK. Results of a multi-institution deformable registration accuracy study (MIDRAS). *Int J Radiat Oncol Biol Phys* 2010;76:583-596.
11. Schmidt MA, Payne GS. Radiotherapy planning using MRI. *Phys Med Biol* 2015;60:R323-R361.
12. Nyholm T, Jonsson J. Counterpoint: Opportunities and challenges of a magnetic resonance imaging-only radiotherapy work flow. *Semin Radiat Oncol* 2014;24:175-180.
13. Kupelian P, Sonke JJ. Magnetic resonance-guided adaptive radiotherapy: A solution to the future. *Semin Radiat Oncol* 2014;24:227-232.
14. Adjeiwaah M, Bylund M, Lundman JA, Karlsson CT, Jonsson JH, Nyholm T. Quantifying the effect of 3T magnetic resonance imaging residual system distortions and patient-induced susceptibility distortions on radiation therapy treatment planning for prostate cancer. *Int J Radiat Oncol* 2018;100:317-324.
15. Persson E, Gustafsson C, Nordström F, et al. MR-OPERA: A multi-center/multi-vendor validation of MRI-only prostate treatment planning using synthetic CT images. *Int J Radiat Oncol* 2017;99:692-700.
16. Lee YK, Bollet M, Charles-Edwards G, et al. Radiotherapy treatment planning of prostate cancer using magnetic resonance imaging alone. *Radiother Oncol* 2003;66:203-216.
17. Thwaites D. Accuracy required and achievable in radiotherapy dosimetry: Have modern technology and techniques changed our views? *J Phys Conf Ser* 2013;444:012006.
18. Schenck JF. The role of magnetic susceptibility in magnetic resonance imaging: MRI magnetic compatibility of the first and second kinds. *Med Phys* 1996;23:815-850.

19. Hargreaves BA, Worters PW, Pauly KB, Pauly JM, Koch KM, Gold GE. Metal-induced artifacts in MRI. *Am J Roentgenol* 2011;197:547-555.
20. Weygand J, Fuller CD, Ibbott GS, et al. Spatial precision in magnetic resonance imaging-guided radiation therapy: The role of geometric distortion. *Int J Radiat Oncol Biol Phys* 2016;96:1304-1316.
21. Sengupta S, Welch EB, Zhao Y, et al. Dynamic B0 shimming at 7 T. *Magn Reson Imaging* 2011;29:483-496.
22. Golay MJE. Field homogenizing coils for nuclear spin resonance instrumentation. *Rev Sci Instrum* 1958;29:313-315.
23. Han H, Song AW, Truong TK. Integrated parallel reception, excitation, and shimming (iPRES). *Magn Reson Med* 2013;70:241-247.
24. Gustafsson C, Nordström F, Persson E, Brynolfsson J, Olsson LE. Assessment of dosimetric impact of system specific geometric distortion in an MRI only based radiotherapy workflow for prostate. *Phys Med Biol* 2017;62:2976-2989.
25. Sun J, Dowling J, Pichler P, et al. MRI simulation: End-to-end testing for prostate radiation therapy using geometric pelvic MRI phantoms. *Phys Med Biol* 2015;60:8.
26. Chen Z, Ma CM, Paskalev K, et al. Investigation of MR image distortion for radiotherapy treatment planning of prostate cancer. *Phys Med Biol* 2006;51:1393-1403.
27. Walker A, Metcalfe P, Liney G, et al. MRI geometric distortion: Impact on tangential whole-breast IMRT. *J Appl Clin Med Phys* 2016;17:7-19.
28. Mohamed ASR, Hansen C, Weygand J, et al. Prospective analysis of in vivo landmark point-based MRI geometric distortion in head and neck cancer patients scanned in immobilized radiation treatment position: Results of a prospective quality assurance protocol. *Clin Transl Radiat Oncol* 2017;7:13-19.
29. Lundman JA, Bylund M, Garpebring A, Thellenberg Karlsson C, Nyholm T. Patient-induced susceptibility effects simulation in magnetic resonance imaging. *Phys Imaging Radiat Oncol* 2017;1:41-45.
30. Zackrisson B, Kjellén E, Söderström K, et al. Mature results from a Swedish comparison study of conventional versus accelerated radiotherapy in head and neck squamous cell carcinoma—The ARTSCAN trial. *Radiother Oncol* 2015;117:99-105.
31. Illerstaam F. Quality assurance of the spatial accuracy of large field of view magnetic resonance imaging [Thesis]; 2014.
32. Beier T, Neely S. Feature-based image metamorphosis. *ACM SIG-GRAPH Comput Graph* 1992;26:35-42.
33. Hopkins JA, Wehrli FW. Magnetic susceptibility measurement of insoluble solids by NMR: Magnetic susceptibility of bone. *Magn Reson Med* 1997;37:494-500.
34. Abbaszadeh K, Heffez LB, Mafee MF. Effect of interference of metallic objects on interpretation of T1-weighted magnetic resonance images in the maxillofacial region. *Oral Surg Oral Med Oral Pathol Oral Radiol Endodontol* 2000;89:759-765.
35. Juchem C, de Graaf RA. B 0 magnetic field homogeneity and shimming for in vivo magnetic resonance spectroscopy. *Anal Biochem* 2017;529:17-29.
36. Insight Segmentation and Registration Toolkit. WarpImageFilter. Available at: https://itk.org/Doxygen/html/classitk_1_1WarpImageFilter.html. Accessed October 2, 2015.
37. Tustison NJ, Gee JC. Introducing Dice, Jaccard, and other label overlap measures to ITK. *Insight J* 2009;2.
38. International Commission on Radiation Units and Measurements. Prescribing, recording and reporting photo beam therapy (Supplement to ICRU Report 50); 1999.
39. Chen L, Price RA, Wang L, et al. MRI-based treatment planning for radiotherapy: Dosimetric verification for prostate IMRT. *Int J Radiat Oncol Biol Phys* 2004;60:636-647.
40. Prabhakar R, Julka PK, Ganesh T, Munshi A, Joshi RC, Rath GK. Feasibility of using MRI alone for 3D radiation treatment planning in brain tumors. *Jpn J Clin Oncol* 2007;37:405-411.
41. Chin AL, Lin A, Anamalayil S, Teo BK. Feasibility and limitations of bulk density assignment in MRI for head and neck IMRT treatment planning. *J Appl Clin Med Phys* 2014;15:100-111.
42. Liney GP, Moerland MA. Magnetic resonance imaging acquisition techniques for radiotherapy planning. *Semin Radiat Oncol* 2014;24:160-168.
43. Wang H, Balter J, Cao Y. Patient-induced susceptibility effect on geometric distortion of clinical brain MRI for radiation treatment planning on a 3T scanner. *Phys Med Biol* 2013;58:465-477.
44. Fransson A, Andreo P, Pötter R. Aspects of MR image distortions in radiotherapy treatment planning. *Strahlenther Onkol* 2001;177:59-73.
45. Stanescu T, Wachowicz K, Jaffray DA. Characterization of tissue magnetic susceptibility-induced distortions for MRIgRT. *Med Phys* 2012;39:7185-7193.
46. Wachowicz K, Stanescu T, Thomas SD, Fallone BG. Implications of tissue magnetic susceptibility-related distortion on the rotating magnet in an MR-linac design. *Med Phys* 2010;37:1714-1721.
47. Crijns SPM, Raaymakers BW, Lagendijk JJW. Real-time correction of magnetic field inhomogeneity-induced image distortions for MRI-guided conventional and proton radiotherapy. *Phys Med Biol* 2011;56:289-297.
48. Sumanaweera TSS, Napel S, Glover S, Song SMM. Quantification of the geometric accuracy of MRI in tissue: A new approach using MRI itself. 1993 IEEE Conf Rec Nucl Sci Symp Med Imaging Conf; 1993;1789-1793.
49. Carlsson Å. Susceptibility effects in MRI and 1 H MRS: The spurious echo artifact and susceptibility measurements (thesis); 2009.
50. Boer VO, Klomp DWJ, Juchem C, Luijten PR, de Graaf RA. Multislice 1H MRSI of the human brain at 7 T using dynamic B0 and B1 shimming. *Magn Reson Med* 2012;68:662-670.
51. Boer VO, Luttje MP, Luijten PR, Klomp DWJ. Requirements for static and dynamic higher order B0 shimming of the human breast at 7 T. *NMR Biomed* 2014;27:625-631.
52. Morrell G, Spielman D. Dynamic shimming for multi-slice magnetic resonance imaging. *Magn Reson Med* 1997;38:477-483.
53. Boer VO, Siero JCW, Hoogduin H, van Gorp JS, Luitjen PR, Klomp DWJ. High-field MRS of the human brain at short TE and TR. *NMR Biomed* 2011;24:1081-1088.
54. Gruetter R. Automatic, localized in vivo adjustment of all first- and second-order shim coils. *Magn Reson Med* 1993;29:804-811.
55. Wyatt J, Hedley S, Johnstone E, et al. Evaluating the repeatability and set-up sensitivity of a large field of view distortion phantom and software for magnetic resonance-only radiotherapy. *Phys Imaging Radiat Oncol* 2018;6:31-38.